

Kinematically Redundant Actuators, a solution for conflicting torque-speed requirements

Verstraten, Tom; Furnémont, Raphaël Guy; Lopez Garcia, Pablo; Rodriguez Cianza, David; Vanderborght, Bram; Lefeber, Dirk

Published in:
International Journal of Robotics Research

DOI:
[10.1177/0278364919826382](https://doi.org/10.1177/0278364919826382)

Publication date:
2019

Document Version:
Accepted author manuscript

[Link to publication](#)

Citation for published version (APA):
Verstraten, T., Furnémont, R. G., Lopez Garcia, P., Rodriguez Cianza, D., Vanderborght, B., & Lefeber, D. (2019). Kinematically Redundant Actuators, a solution for conflicting torque-speed requirements. *International Journal of Robotics Research*, 38(5), 612-629. <https://doi.org/10.1177/0278364919826382>

Copyright

No part of this publication may be reproduced or transmitted in any form, without the prior written permission of the author(s) or other rights holders to whom publication rights have been transferred, unless permitted by a license attached to the publication (a Creative Commons license or other), or unless exceptions to copyright law apply.

Take down policy

If you believe that this document infringes your copyright or other rights, please contact openaccess@vub.be, with details of the nature of the infringement. We will investigate the claim and if justified, we will take the appropriate steps.

Kinematically Redundant Actuators, a solution for conflicting torque-speed requirements

International Journal of Robotics
Research
XX(X):1–17
©The Author(s) 2018
Reprints and permission:
sagepub.co.uk/journalsPermissions.nav
DOI: 10.1177/ToBeAssigned
www.sagepub.com/



Tom Verstraten¹, Raphael Furnémont¹, Pablo Lopez-Garcia¹, David Rodriguez-Cianca¹, Bram Vanderborght¹ and Dirk Lefeber¹

Abstract

Robots often switch from highly dynamic motion to delivering high torques at low speeds. The actuation requirements for these two regimes are very different. As a consequence, the average efficiency of the actuators is typically much lower than the efficiency at the optimal working point. A potential solution is to use multiple motors for a single motor joint. This results in a redundant degree of freedom, which can be exploited to make the system more efficient overall. In this work, we explore the potential of kinematically redundant actuators in dynamic applications. The potential of a kinematically redundant actuator with two motors is evaluated against a single-motor equivalent in terms of operating range, maximum acceleration and energy consumption. We discuss how the comparison is influenced by the design of the actuator and the way how the power is distributed over the input motors. Our results support the idea that kinematically redundant actuators can resolve the conflicting torque-speed requirements typical of robots.

Keywords

Over-actuated systems, Redundant actuation, Energy efficiency, Actuator Dynamics

1 Introduction

Mobile robots and wearable robotic devices are gradually entering our everyday lives. Such devices should have a long-lasting autonomy, without paying the price of carrying a heavy and bulky battery pack. The best way to achieve this is to reduce the energy consumption of the robot itself. Fortunately, electric motors, one of the prominent actuation technologies, offer very high efficiencies at their nominal working point. A motor's efficiency, however, varies strongly with speed and torque (Tucker and Fite 2010; Verstraten et al. 2015). This is an issue in robotics, where actuators are required to operate at a wide range of working points. As a result, their motors tend to be used very inefficiently. In the MIT Cheetah robot, for example, up to 68% of the total energy was consumed by heating of the motor windings (Seok et al. 2013). Designs focusing on the reduction of motor losses can significantly improve the overall efficiency of a device. With such an approach, Brown and Ulsoy (2013) managed to decrease the energy consumption of a passive-assist device by 25%. No less than 90% of the energy savings was attributed to a more efficient use of the motor.

A well-chosen transmission can help by mapping the expected working points as closely as possible to energy-efficient part of the motor's operating range. Nevertheless, transmissions with fixed reductions can only do so much when the working points are widely spread over the operating range. This is a typical problem of robots interacting with their environment. Tasks such as turning knobs or manipulating high payloads often require high torques from the robot's actuators at low output speeds. As a consequence, the actuators will consist of strong motors with high reductions. When the payload is removed and the

manipulator is brought back to its initial position, however, the requirement changes to delivering high speeds at low torques. The speed with which the arm can move will then be limited by the high reflected inertia resulting from the high-torque design (Babin et al. 2014).

The conflicting torque-speed requirements resulting from a loaded and a no-load phase are also a problem in legged robotics. During the stance phase, the leg needs to carry the robot's weight, requiring high motor torques. When the foot is lifted from the ground (swing phase), the required motor torque drops considerably since the leg is now only moving its own inertia, but the motors need to work at higher speeds. This has serious consequences for the sizing and energy efficiency of the actuators. A human ankle requires hardly any power during the swing phase of walking gait, but when a motor performs the same motion, it displays considerable peak powers in this phase, even if springs are used to alleviate the requirements (Hitt et al. 2010; Verstraten et al. 2017).

A potential solution to these problems is to use variable transmissions (Sugar and Holgate 2013) or, more generally, to actuate a joint with not one, but two motors. The second motor then creates an additional, redundant, degree

¹Robotics and Multibody Mechanics Research Group (R&MM), Vrije Universiteit Brussel, Belgium. The R&MM Research Group is a part of Flanders Make.

Corresponding author:

Tom Verstraten,
Department of Mechanical Engineering (MECH),
Vrije Universiteit Brussel / Flanders Make,
Pleinlaan 2,
1050 Elsene
Email: tom.verstraten@vub.be

of freedom, which can be exploited to distribute the power requirements among both motors in the most energy-efficient way. With a proper design and proper control, the overall quasi-static efficiency of such an actuator can be better than that of a single motor with gear reducer (Verstraten et al. 2018). In dynamic tasks, however, the inertia of the drivetrain has a strong influence on the power flow through the motor (Verstraten et al. 2016) and may lead to high Joule losses (Plooij and Wisse 2012). This issue is very relevant for redundant actuators, considering that it consists of not one, but at least two motors. Still, the important but difficult question of how this affects their energy consumption and the ideal power distribution between the motors, is yet to be answered. This work contributes towards solving this pertinent issue by providing several insights from theory and experiments on a kinematically redundant actuator.

We start the paper by giving an overview of different types of redundant actuators, focusing on previous research on kinematically redundant actuators (Section 2). Next, we establish the equations for a kinematically redundant actuator and its optimal control (Section 3). We then discuss the design of such an actuator in terms of operating range, reflected inertia, maximum acceleration and energy consumption in a dynamic task (Section 4). In Section 5, we experimentally validate the dynamic model of the actuator by forcing harmonic oscillations onto an inertial load. Optimal control is used to distribute the required speed over both motors in an energy-optimal way. The findings of the work are summarized in an overview of the advantages and disadvantages of the DMA (Section 6). We finish by concluding that kinematically redundant actuators can provide a solution for conflicting torque-speed requirements (Section 7).

2 Types of redundant actuators

Redundancy on robot-level is a well-studied topic, with a vast array of literature on over-actuated robotic arms. Redundancy on joint-level has received little attention in comparison. In this section, we provide an overview of existing concepts for redundant actuators. We divide them into four classes: statically redundant actuators, kinematically redundant actuators, Variable Stiffness Actuators and actuators with Variable Transmissions.

2.1 Statically redundant actuators

In a *statically redundant actuator*, an infinite number of input motor torques result in the same output torque (Müller 1982). This can be achieved in a very simple way, by coupling multiple motors to the same driveshaft. In such an arrangement, the output torque is the sum of both motor-gearbox torques. The torque that can be delivered by a motor increases with its mass to the power 1.25 (Haddadin et al. 2012). Consequently, using one large motor will generally lead to a more compact and lightweight design than two smaller motors on the same driveshaft.

Despite their unfavorable scaling with mass, statically redundant actuators may have benefits in terms of control performance and energy consumption. In the Parallel-Coupled Micro-Macro actuator concept proposed by Morrell and Salisbury (1998), a small motor is coupled directly to

the load, in addition to a larger motor coupled through a compliant transmission. This actuator exhibited a good force control bandwidth and excellent force fidelity. Peak impact force, force distortion and backdrivability were also found to be better than a single-motor actuator. When combined with springs and locking mechanisms, statically redundant actuators can also offer considerable benefits in terms of energy consumption. An example is the +SPEA actuator proposed by Mathijssen et al. (2016), which consists of four motors with series springs, connected to a single output shaft. Controllable brakes allow the motors to be locked, such that springs in series with the motors act as parallel springs on the output shaft. In a blocked output experiment, this actuator managed a fourfold decrease in energy consumption compared to a single-motor alternative.

2.2 Kinematically redundant actuators

An actuator is *kinematically redundant* if its output speed is not uniquely determined by the speeds of the input motors (Müller 1982). One way of achieving this is to couple two motors to a single output through a differential. In this case, the output speed $\dot{\theta}_o$ is a linear combination of the input speeds $\dot{\theta}_1$ and $\dot{\theta}_2$:

$$\dot{\theta}_o = R_1 \dot{\theta}_1 + R_2 \dot{\theta}_2 \quad (1)$$

with coefficients R_1 and R_2 depending on the design of the differential. The static output torque, however, is divided over both inputs in a fixed ratio, determined by design.

In principle, any type of differential can be chosen to couple both motors. Differential mechanisms that have been proposed include a bevel gear differential (Hu et al. 2015; Fumagalli et al. 2014), a two-stage planetary gear differential (Fauteux et al. 2010; Gao et al. 2016) and a differential based on harmonic drives (Tagliamonte et al. 2010; Wolf and Hirzinger 2008). The most common concept by far is one that employs a planetary differential. Here, the output and the two inputs of the actuator can be assigned to any of the three output shafts of the differential. Assuming that the motors are grounded, this can be done in three possible ways. If one of the motors is allowed to be mounted to a movable component, however, 12 more actuator topologies can be created (Babin et al. 2014).

To the authors' knowledge, the first roboticists to suggest the use of a kinematically redundant actuator were Ontañón Ruiz et al. (1998), with the aim of reducing stiction. Here, the carrier and the sun of the planetary differential were used as inputs, and the load was coupled to the output. Several important theoretical contributions about this specific configuration were made by Rabindran and Tesar. In their analysis of power flows and efficiency (Rabindran and Tesar 2008), they concluded that the efficiency of this type of actuator decreases when the reduction ratio of the planetary differential increases. Furthermore, they found that the reflected inertia of the actuator has no upper bound, while it can never be lower than the inertias of both input actuators. Another study (Rabindran and Tesar 2007) discussed the cross-coupling in the inertia matrix. The authors argued that the coupling should be minimized by design, because it causes the actuators to fight each other's acceleration. In addition to these theoretical works, Rabindran and Tesar

(2014) also showed the potential of the concept in terms of safe response to collisions.

Another configuration places the load on the carrier, and uses the sun and ring as inputs. This topology was used for the first time by Kim et al. (2007, 2010), where one motor was used to control the output position and the other to control the stiffness. Later, Lee and Choi (2012) explored the possibility of shaping the actuator's operating range more favorably than that of a regular motor. In their concept, worm gears were used to prevent the motors from being backdriven. This makes their concept unsuitable for applications in robotics. More recently, Girard and Asada (2015) presented a similar actuator where the worm gears were replaced by controllable brakes. For this actuator, they developed several control strategies to divide the required power over the motors and to deal with the holding brakes (Girard and Asada 2016, 2017). Much work has also been done on impedance control (Nagai et al. 2009). A problem with these actuators in impedance control is that, in order to obtain high bandwidths, motors are required that are able to deliver high torques, but have low inertias. In order to meet these contradicting requirements, Nagai et al. (2010) proposed to equip one of both motors with a parallel spring. Nevertheless, the usage of springs in kinematically redundant actuators is quite rare, with the exception of variable stiffness actuators.

2.3 Variable Stiffness Actuators

Variable Stiffness Actuators (VSAs) are a variant of Series Elastic Actuators, where the stiffness can be varied. In case of a rotational actuator, they can be represented by following idealized equation:

$$\theta_{out} = \theta_1 + \frac{T_{out}}{k(\theta_2)} \quad (2)$$

where θ_{out} and T_{out} represent the output position and torque, and θ_1 and θ_2 are the input positions of the primary and secondary motor. Equation (2) shows that variable stiffness $k(\theta_2)$ changes the kinematic relationship between the primary motor and the output. The variable stiffness $k(\theta_2)$ is thus the redundant degree of freedom. Although exceptions exist, it is regulated by a secondary motor in the vast majority of cases (Groothuis et al. 2016).

VSAs can be classified as kinematically redundant actuators if the output torque uniquely defines the torques required from the input motors. For most VSA designs, this is not the case. For an extensive overview of VSA designs and their advantages, we refer to the excellent review papers by Vanderborght et al. (2013) and Tagliamonte et al. (2012).

2.4 Variable transmissions

Another way to add a redundant degree of freedom is to use a variable transmission. The actuator can then be described with following equations:

$$\theta_{out} = \frac{\theta_1}{n(\theta_2)} \quad (3)$$

$$T_{out} = n(\theta_2)T_1 \quad (4)$$

In this type of actuator, the variable gear ratio – which we assume to be controlled by a secondary motor – creates the

redundant degree of freedom. The variable gear ratio affects both the torque and speed, resulting in coupled kinematic and static redundancy.

Over the years, variable transmissions have proven their potential to reduce the energy consumption of cars (Carbone et al. 2001) and wind turbines (Mangialardi and Mantriota 1994). These results have sparked interest from researchers in robotics. Variable transmissions show great potential in the field of legged locomotion, prosthetics and exoskeletons. They can be used to shape a motor's speed-torque curve more favorably for its use in ankle prostheses, enabling a more compact actuator design (Sugar and Holgate 2013). Combined with energy buffers such as springs (Stramigioli et al. 2008) or flywheels (Dresscher et al. 2015), they can also form very efficient actuation units. Simulations have shown that a knee actuator consisting of an IVT with a flywheel could reduce the actuator's energy consumption by 85% in walking (Aló et al. 2015). Similar reductions have been reported for an IVT combined with a spring (Mooney and Herr 2013). In addition to the improved energy efficiency, variable transmissions can also help to reduce the weight of knee prostheses (Lenzi et al. 2017).

The most common CVT types, belt and chain CVTs and toroidal CVTs, tend to have issues with rapid changes in gear ratio (Srivastava and Haque 2009), while also being heavy and bulky (Everarts et al. 2015). Small-size CVTs exist, but often have the disadvantage of having a limited range of motion. Furthermore, they are often friction-based, limiting their torque transmission capability (Everarts et al. 2015). Consequently, the search for the ideal CVT for robotics is still an ongoing research topic (Belter and Dollar 2014; Everarts et al. 2015; Lenzi et al. 2017; Kembaum et al. 2017; Dresscher et al. 2017).

3 Equations

In this work, we study a kinematically redundant actuator with planetary differential, which we will refer to as "Dual-Motor Actuator" (DMA) in accordance with Verstraten et al. (2018). A schematic is depicted in Fig. 1. The planetary differential is essentially the same as a planetary gearbox, but the ring is used as a secondary input instead of being fixed to ground. Just like in a regular planetary gearbox, the output shaft is connected to the carrier, and the sun is used as a second input. Other configurations of input and output shafts are possible, but this specific configuration offers the highest reductions.

3.1 Kinematics

The relationship between the output speed $\dot{\theta}_o$ and the input speeds $\dot{\theta}_S$ and $\dot{\theta}_R$ of the sun and ring motor, respectively, is given by (Müller 1982)

$$\dot{\theta}_o = \mathbf{J} \begin{bmatrix} \dot{\theta}_S \\ \dot{\theta}_R \end{bmatrix} \quad (5)$$

$$\mathbf{J} = \begin{bmatrix} \frac{1}{n_S} \frac{1}{1+\rho} & \frac{1}{n_R} \frac{\rho}{1+\rho} \end{bmatrix} \quad (6)$$

with n_S and n_R the additional reductions provided by the planetary gearboxes in the ring and sun drivetrain (see Fig. 1). The dimensionless ratio ρ in Eq. (5) is defined as

$$\rho = r_R/r_S \quad (7)$$

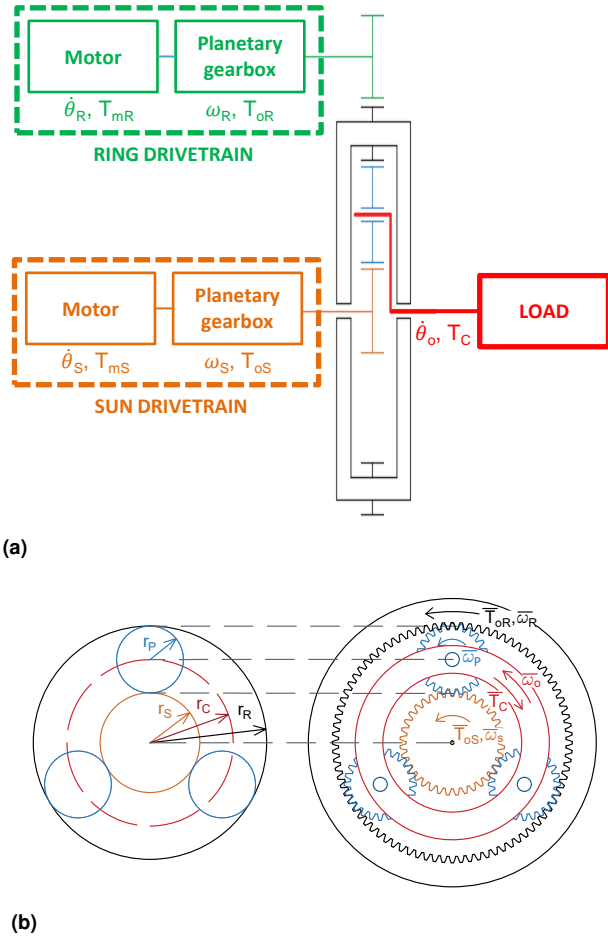


Figure 1. Schematic of the kinematically redundant actuator with planetary differential. (a) Overview of the complete actuator, (b) Planetary differential with definitions of angular velocities and torques.

in which r_R and r_S are the radii of the pitch circles of the ring and sun gear, respectively, of the planetary differential. Eq. (5) corresponds to the general equation for a kinematically redundant actuator (1) with $R_1 = \frac{1}{n_S} \frac{1}{1+\rho}$ and $R_2 = \frac{1}{n_R} \frac{\rho}{1+\rho}$. Because Eq. (5) cannot be inverted, we define the speed ratio γ as

$$\gamma = \frac{1}{n_R} \frac{\rho}{1+\rho} \frac{\dot{\theta}_R}{\dot{\theta}_o} \quad (8)$$

This allows us to rewrite the relationships between the input speeds and output speed as

$$\begin{bmatrix} \dot{\theta}_S \\ \dot{\theta}_R \end{bmatrix} = \mathbf{Q} \dot{\theta}_o \quad (9)$$

$$\mathbf{Q} = \begin{bmatrix} n_S (1+\rho) (1-\gamma) \\ n_R \frac{(1+\rho)}{\rho} \gamma \end{bmatrix} \quad (10)$$

By differentiation, we find the accelerations

$$\begin{bmatrix} \ddot{\theta}_S \\ \ddot{\theta}_R \end{bmatrix} = \mathbf{Q} \ddot{\theta}_o + \begin{bmatrix} -n_S (1+\rho) \\ n_R \frac{(1+\rho)}{\rho} \end{bmatrix} \dot{\theta}_o \dot{\gamma} \quad (11)$$

3.2 Dynamics

In a lossless planetary differential, the torques applied to the ring and sun gear, T_{oR} and T_{oS} , are linked through the

equations

$$T_{oR} = \frac{r_R}{r_S} T_{oS} = \rho T_{oS} \quad (12)$$

In order to model the losses, we introduce the efficiency function of the planetary gear differential:

$$C_{PG} = \eta_{PG}^{\text{sgn}[T_C (\frac{\dot{\theta}_S}{n_S} - \dot{\theta}_C)]} \quad (13)$$

where η_{PG} denotes the meshing efficiency of the sun and ring gear with the planets. The efficiency functions of the gearboxes are given by

$$C_\lambda = \eta_\lambda^{-\text{sgn}(T_{o\lambda} \dot{\theta}_\lambda)} \quad (14)$$

where η_λ represents the catalog efficiency of the respective gearbox ($\lambda = R, S$). Defining the input vector in dual-motor operation as $\mathbf{T}_{2m} = (T_{mS}, T_{mR})^T$, with T_{mS} and T_{mR} the motor torques of the sun and ring motor, respectively, we can write

$$\mathbf{T}_{2m} = \mathbf{A} \dot{\mathbf{x}} + \mathbf{B} \mathbf{x} + \mathbf{C} \text{sgn}(\mathbf{x}) + \mathbf{D} (T_o + T_{CC} \text{sgn}(\mathbf{J} \mathbf{x})) \quad (15)$$

where T_o is the output torque, \mathbf{x} the state vector

$$\mathbf{x} = \begin{bmatrix} \dot{\theta}_S \\ \dot{\theta}_R \end{bmatrix} \quad (16)$$

and

$$\mathbf{A} = \begin{bmatrix} J_S & 0 \\ 0 & J_R \end{bmatrix} + J_C \mathbf{D} \begin{bmatrix} \frac{1}{n_S} \frac{1}{1+\rho} & \frac{1}{n_R} \frac{\rho}{1+\rho} \end{bmatrix} \quad (17)$$

$$\mathbf{B} = \begin{bmatrix} \nu_S & 0 \\ 0 & \nu_R \end{bmatrix} + \nu_C \mathbf{D} \begin{bmatrix} \frac{1}{n_S} \frac{1}{1+\rho} & \frac{1}{n_R} \frac{\rho}{1+\rho} \end{bmatrix} \quad (18)$$

$$\mathbf{C} = \begin{bmatrix} T_{CS} & 0 \\ 0 & T_{CR} \end{bmatrix} \quad (19)$$

$$\mathbf{D} = \begin{bmatrix} \frac{C_S}{n_S} (\rho C_{PG} + 1)^{-1} \\ \frac{C_R}{n_R} \left(\frac{1}{\rho C_{PG}} + 1 \right)^{-1} \end{bmatrix} \quad (20)$$

The parameters are defined in Table 1 and 2. The inertia of the planetary differential's planets is assumed to be negligible compared to that of the sun, ring and carrier, which have an entire drivetrain attached to them. Friction is accounted for in Eq. (15) by Coulomb friction terms $\mathbf{C} \text{sgn}(\mathbf{x})$ (friction at input) and $T_{CC} \text{sgn}(\mathbf{J} \mathbf{x})$ (friction at output) and a viscous friction term $\mathbf{B} \mathbf{x}$ (for both input and output). This classical model captures the main effects of friction in mechatronic systems (Olsson et al. 1998). Friction coefficients were obtained experimentally in previous work (Verstraten et al. 2018). A full derivation of the matrix \mathbf{D} , which contains the gearbox efficiency function C_{PG} , can also be found in this work.

3.3 Motor equations

The motor currents I_λ and voltages U_λ can be calculated with following motor model:

$$I_\lambda = \frac{1}{k_{T\lambda}} T_{m\lambda} \quad (21)$$

$$U_\lambda = k_{T\lambda} \dot{\theta}_\lambda + R_\lambda I_\lambda \quad (22)$$

Table 1. Parameters for the planetary differential. Friction parameters were obtained from steady-state measurements, as described in (Verstraten et al. 2018). The inertia J_C was retrieved from datasheet information and CAD drawings.

| | |
|--|-------------------------|
| ρ | 9 |
| Efficiency of planetary differential η_{PG} | 88 |
| Carrier inertia J_C | 12e-6 kg m ² |
| Carrier viscous friction ν_C | 1e-3 Nm/(rad/s) |
| Coulomb friction of carrier T_{CC} | 0.1033 Nm |

with $k_{T\lambda}$ the torque constant and R_λ the winding resistance of the respective motor ($\lambda = R, S$). The electrical powers $P_{elec,\lambda}$ of the sun and ring motor are given by

$$P_{elec,\lambda} = U_\lambda \cdot I_\lambda \quad (23)$$

Finally, the total electrical power P_{elec} is the sum of the sun and ring motor powers:

$$P_{elec} = P_{elec,S} + P_{elec,R} \quad (24)$$

3.4 Constraints

Defining the maximum motor speed $\dot{\theta}_{\lambda max}$, the maximum peak current $I_{\lambda max, peak}$ and the maximum continuous torque $T_{\lambda max, cont}$ ($\lambda=R,S$), we can write following constraints:

$$|\dot{\theta}_\lambda| < \dot{\theta}_{\lambda max} \quad (25)$$

$$|I_\lambda| < I_{\lambda max, peak} \quad (26)$$

$$\text{rms}(T_\lambda) < T_{\lambda max, cont} \quad (27)$$

The maximum motor speed and maximum continuous torque can be found in the motor datasheets supplied by the manufacturer. The peak current is limited by short-term heating of the motor windings, but also by the maximum current output of the controller's power stage. We will take the latter to define $I_{\lambda max, peak}$. Furthermore, the supply voltage U_{max} puts a limit on the speeds that can be achieved at a certain torque:

$$k_{T\lambda}\dot{\theta}_\lambda + R_\lambda I_\lambda < U_{max} \quad (28)$$

3.5 Optimal control

As explained in Section 2.2, the actuator's kinematic redundancy implies that the speeds of the two input motors can be chosen freely, even if the output speed is defined. This property can be used to fulfill a secondary objective in addition to the primary objective of, e.g., tracking a desired output force or position.

In this work, more specifically in Section 4.4, the primary objective is to track an output speed, while the secondary objective is to minimize the actuator's electrical energy consumption. This requires solving an optimal control problem (OCP) which can be formulated as:

$$\begin{aligned} \min_u \left(J_E = \int_{t_0}^{t_f} g(\mathbf{x}, \mathbf{u}, t) dt \right) \\ \dot{\mathbf{x}} = \mathbf{f}(\mathbf{x}, \mathbf{u}, t) \\ h(\mathbf{x}, \mathbf{u}, t) = 0 \\ \mathbf{c}_{\min} \leq \mathbf{c}(\mathbf{x}, \mathbf{u}, t) \leq \mathbf{c}_{\max} \end{aligned} \quad (29)$$

Generally speaking, the goal is to find the control set $\mathbf{u} = (I_S, I_R)^T$ which minimizes the cost J_E , defined as the integral of a cost function $g(\mathbf{x}, \mathbf{u}, t)$ over a time interval $[t_0, t_f]$, with the state vector \mathbf{x} defined previously by Eq. (16). In this work, we wish to optimize the efficiency of the DMA with respect to a reference drivetrain. The cost function is thus the total electrical power, which can be written as the sum of the mechanical power $\mathbf{x}^T \mathbf{K} \mathbf{u}$, which includes all friction losses, and the Joule losses $\mathbf{u}^T \mathbf{R} \mathbf{u}$:

$$\begin{aligned} g(\mathbf{x}, \mathbf{u}, t) &= \mathbf{x}^T \mathbf{K} \mathbf{u} + \mathbf{u}^T \mathbf{R} \mathbf{u} \\ \mathbf{K} &= \begin{bmatrix} k_{TS} & 0 \\ 0 & k_{TR} \end{bmatrix} \\ \mathbf{R} &= \begin{bmatrix} R_S & 0 \\ 0 & R_R \end{bmatrix} \end{aligned} \quad (30)$$

Although simpler cost functions based on motor torque (Uemura and Kawamura 2009; Roozing et al. 2016; Girard and Asada 2016) or mechanical power (Grimmer et al. 2014; Paryanto et al. 2015; Mohammed et al. 2016) may also lead to close-to-optimal behavior in terms of energy consumption (Verstraten et al. 2017), Eq. (30) ensures the highest accuracy in terms of reducing the actual electrical energy consumption. This claim was validated in Remy et al. (2012), where different cost functions were used in an optimal control formulation to generate running gaits for a one-legged robotic hopper.

The system has two constraints. First, there is the dynamics of the system, which can be expressed as a set of differential equations $\dot{\mathbf{x}} = \mathbf{f}(\mathbf{x}, \mathbf{u}, t)$. The dynamics of the system were given by Eq. (15) and can be rewritten as

$$\dot{\mathbf{x}} = \mathbf{A}^{-1} (\mathbf{K} \mathbf{u} - \mathbf{B} \mathbf{x} - \mathbf{C} \text{sgn}(\mathbf{x}) - \mathbf{D} (T_o(t) + T_{CC} \text{sgn}(\mathbf{J} \mathbf{x}))) \quad (31)$$

Second, a path constraint is $h(\mathbf{x}, \mathbf{u}, t) = 0$ is introduced. It forces the output of the DMA to track the imposed output speed $\dot{\theta}_o$, which is the primary objective of the controller. The path constraint is derived from Eq. (5), which describes the kinematics of the DMA:

$$h(\mathbf{x}, \mathbf{u}, t) = \dot{\theta}_o(t) - \left[\frac{1}{n_S(1+\rho)} \quad \frac{\rho}{n_R(1+\rho)} \right] \mathbf{x} = 0 \quad (32)$$

Finally, we would like to ensure that the control set does not lead to saturation of the actuator. We will thus add inequality constraints of the form

$$\mathbf{c}_{\min} \leq \mathbf{c}(\mathbf{x}, \mathbf{u}, t) \leq \mathbf{c}_{\max} \quad (33)$$

where

$$\mathbf{c}(\mathbf{x}, \mathbf{u}, t) = \begin{bmatrix} \mathbf{x} \\ \mathbf{K} \mathbf{u} \\ \mathbf{K} \mathbf{x} + \mathbf{R} \mathbf{u} \end{bmatrix} \quad (34)$$

contains, respectively, the maximum motor speeds, maximum motor torques, and maximum output voltages (see 3.4). The vectors \mathbf{c}_{\min} and \mathbf{c}_{\max} are given by

$$\mathbf{c}_{\max} = -\mathbf{c}_{\min} = \begin{bmatrix} \dot{\theta}_{Smax} \\ \dot{\theta}_{Rmax} \\ \sqrt{2} \cdot T_{Smax, cont} \\ \sqrt{2} \cdot T_{Rmax, cont} \\ U_{max} \\ U_{max} \end{bmatrix} \quad (35)$$

Table 2. Parameters for the drivetrains of the dual-motor actuator and for the reference drivetrain. Friction parameters were obtained from steady-state measurements, as described in (Verstraten et al. 2018). The inertias J_S , J_R and J_{ref} were obtained from datasheet information and CAD drawings.

| | Reference drivetrain ($\lambda = ref$) | Sun drivetrain ($\lambda = S$) | Ring drivetrain ($\lambda = R$) |
|---|---|-------------------------------------|--------------------------------------|
| Drivetrain inertia J_λ | 1.38e-4 kg m ² | 1.6e-5 kg m ² | 9.5e-6 kg m ² |
| Viscous friction coefficient ν_λ | 1.0e-3 Nm/(rad/s) | 1.5e-5 Nm/(rad/s) | 1.5e-12 Nm/(rad/s) |
| Coulomb friction coefficient $T_{C\lambda}$ | 0.040 Nm | 0.0080 Nm | 0.0061 Nm |
| Motor | Maxon RE65 | Maxon RE40 | Maxon RE35 |
| Nominal power P_{nom} | 250 W | 150 W | 90 W |
| Nominal torque $T_{\lambda max, cont}$ | 485 mNm | 177 mNm | 101 mNm |
| Max. speed $\omega_{\lambda max}$ | 3000 rpm | 12000 rpm | 12000 rpm |
| Terminal resistance R_λ | 82.1 m Ω | 299 m Ω | 583 m Ω |
| Torque constant $k_{T\lambda}$ | 55.4 mNm/A | 30.2 mNm/A | 19.4 mNm/A |
| Gearbox | Maxon GP82 | Maxon GP42 | Maxon GP42 |
| Gear ratio n_λ | 35 | 15 | 129 |
| Gearbox efficiency η_λ | 70 % | 81 % | 68 % |

Equation (33) ensures that constraints (25), (27) and (28) are respected. To apply constraint (27) it was assumed that the motor torque follows a sinusoidal trajectory. In that case, the peak torque will be $\sqrt{2}$ times higher than the rms torque. Therefore, by limiting the motor torques to $\sqrt{2} \cdot T_{\lambda max, cont}$, we effectively limit the rms torque to $T_{\lambda max, cont}$. As we will show in Section 5, the assumption of a sinusoidal motor torque (current) is justified. Finally, constraint (26) is, in this specific case, less strict than constraint (27), which is why it is not a part of the inequality (33).

The OCP was solved using GPOPS-II (Patterson and Rao 2014). This software transcribes the OCP into a large scale nonlinear programming problem (NLP) and then solves the problem by using the NLP solver IPOPT (Biegler and Zavala 2009).

4 Design analysis

In previous work, we showed that the DMA could statically deliver high torques (20 Nm) at high speeds (100 rpm) while being lighter and more compact than a traditional motor with gear reducer (Verstraten et al. 2018). But how does the actuator perform in dynamic applications? In order to answer this question, we compare a specific DMA design to reference drivetrain composed of a motor with gear reducer. The DMA has a 150W DC motor with 15:1 reduction (sun) and a 90W DC motor with 129:1 reduction (ring) as inputs. The reference drivetrain, a 250W DC motor with 35:1 gear reduction, is designed to cover approximately the same steady-state operating range while respecting the constraints listed in Section 3.4. The supply voltage U_{max} is assumed to be 30V for both motors. Parameters of the drivetrains are listed in Table 2. The parameters of the planetary differential used in the DMA are listed in Table 1.

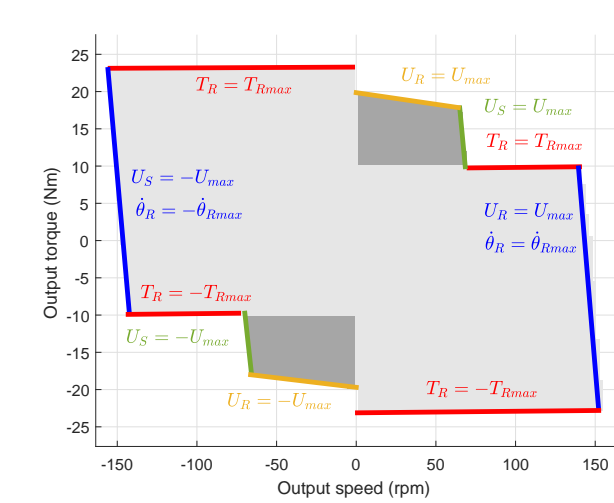
Unlike in Girard and Asada (2015) and Verstraten et al. (2018), the DMA analyzed in this work does not feature brakes or other non-backdrivable mechanisms such as the worm gears in Lee and Choi (2012). In these designs, the operating range of the DMA can be turned into an L-shape, i.e. with a high-speed low-torque region and a high-torque low-speed region (Lee and Choi 2012). Such an L-shaped operating range is particularly useful for robotic

ankles. Here, motors either provide high torques or high speeds, but never reach their maximum power output (Sugar and Holgate 2013). By using a DMA with brakes, the unused part of the operating range can be eliminated. As a result, the DMA can be composed of small motors, reducing the overall weight and size of the actuator (Girard and Asada 2015) and improving its energy efficiency over that of a single-motor alternative (Verstraten et al. 2018). However, non-backdrivable mechanisms also have several disadvantages. Firstly, they complicate the control of the actuator, as they introduce discontinuities in the system. If online control is desired, advanced control algorithms will be needed in order to deal with these discontinuities. Second, controllable brakes will require a certain energy input to keep them engaged or disengaged, or to switch between those states. Moreover, they also add weight, volume and cost to the actuation system. Whether the brakes are actually worthwhile therefore depends on the benefit that can be gained from them in terms of energy efficiency, and to what extent they enable a reduction of size and weight of the individual drivetrains. For these reasons, we chose to study a system without brakes, which is more likely to be preferred whenever simplicity and cost are important.

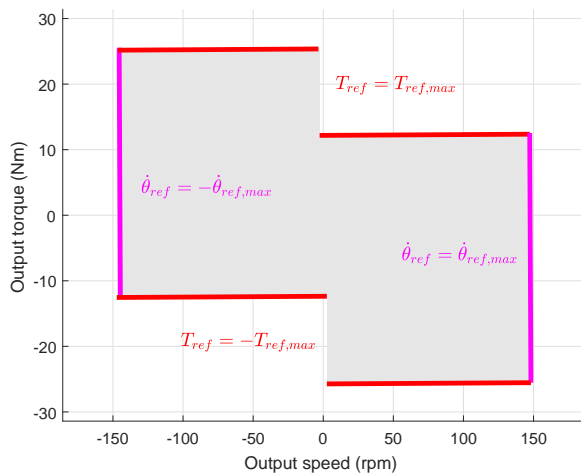
We start this section by comparing the operating ranges of the two motors. Next, we provide a theoretical discussion of the reflected inertia of a DMA and its impact on the maximum output acceleration that can be achieved with the actuator. We conclude the section by comparing the DMA's efficiency to that of the reference actuator, in a task where sinusoidal oscillations are applied to an inertial load.

4.1 Operating range

The operating range of a drivetrain consisting of a motor and gearbox is limited by the constraints listed in Section 3.4. All of these constraints are a function of speed and torque, which is why the operating range is typically represented on a speed-torque plane. The *steady-state operating range* of a drivetrain can therefore be defined as all possible combinations of speed and torque for which the motor and gearbox constraints are respected. For the kinematically redundant DMA, the steady-state operating range is defined



(a) DMA



(b) Reference drivetrain

Figure 2. Steady-state operating range of the (a) dual-motor actuator, compared to (b) the reference motor. Specifications of the actuators are listed in Tables 1 and 2. The constraints associated with the boundaries are indicated on the figure. The reference drivetrain was designed to cover roughly the same operating range. The dual-motor, however, is capable of delivering high torques at low speeds (dark zone), where the reference drivetrain cannot be used.

by all combinations of speed and torque for which at least one speed ratio γ can be found which does not violate the motor and gearbox constraints. In accordance with this definition, Fig. 2 shows the operating range of the DMA and the reference drivetrain it is being compared to.

With non-backdrivable mechanisms, it would be possible to exploit the full torque range of either branch, enabling the construction of the L-shaped operating range described in the introduction of this section. The maximum output torque that can be provided by a DMA without brakes is, however, limited by the weakest branch, in this case the ring branch. This was explained mathematically in Verstraten et al. (2018). In Fig. 2a, many of the operating region's boundaries are, indeed, determined by the maximum continuous torque of the ring drivetrain.

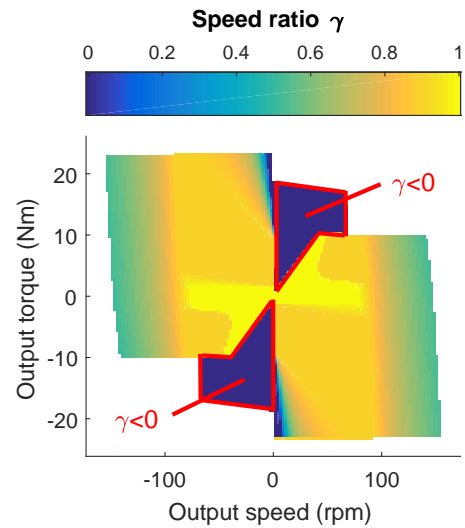


Figure 3. Optimal speed ratio in steady-state conditions. The map is obtained by means of a parameter sweep on the ring speed (step size 1 rpm) through its entire range of permissible speeds. All speed ratios are between 0 and 1, except for the dark blue zone, where the speed ratio is just below zero. The optimal speed ratio is close to one in a large part of the operating range, indicating that the ring drivetrain is more efficient than the sun drivetrain. For high speeds, the optimal speed ratio drops, as the ring motor alone cannot provide the required output speed.

While previous works (Lee and Choi 2012; Girard and Asada 2015) have reported on the working range in quadrant I, we also offer a view on the negative power quadrants II and IV, which are also of importance in the field of robotics. The main difference between those quadrants is the role of friction and gearbox losses. In the positive power quadrants, these losses increase the torque demanded from the motor. When power is flowing from the load to the motor, however, friction and gearbox losses relieve the motor's torque requirement by absorbing some of the incoming negative power. For example, due to the gearbox alone, a motor equipped with a gearbox with efficiency η_{gb} can deliver $1/\eta_{gb}^2$ times more torque in the negative power quadrants II and IV than in the positive quadrants I and III. This is also visible in Fig. 2b where, in the negative power quadrants, the reference motor can reach torques that are approximately $1/\eta_{ref}^2 = 2$ times higher than in the positive power quadrants.

Because the voltage is sufficiently high, the torque-speed line does not limit the operating range of the reference actuator. As a result, the operating range is square in each of the four quadrants, restricted by only the maximum continuous torque $T_{ref,max,cont}$ and the maximum speed $\dot{\theta}_{ref,max}$. The operating range of the DMA is quite similar in size and shape, except for two additional areas in quadrants I and III, marked in dark grey in Fig. 2a. The appearance of these areas can be understood by looking at the optimal speed ratio (Fig. 3). This figure shows that, in the dark grey areas, the speed ratio γ is just below zero. According to Eq. (8), this implies that the ring speed has the opposite sign of the sun and output speeds. Because, according to the definitions in Fig. 1, all torques on the planetary differential have the same sign, a ring speed of opposite sign also indicates a power

Table 3. Inertias of the drivetrains and their individual components, reflected to the motor. Because the differential was constructed from an off-the-shelf gearbox, only the total inertia of the differential is known; the separate inertias of the ring and sun were estimated based on datasheet information and design considerations.

| | Reference | Sun | Ring |
|--------------|--------------------------|-------------------------|-------------------------|
| Motor | 1290 gcm ² | 142 gcm ² | 79.2 gcm ² |
| Gearbox | 88 gcm ² | 15 gcm ² | 15 gcm ² |
| Differential | - | 1.42 gcm ² | 0.87 gcm ² |
| Total | 1.38e-4 kgm ² | 1.6e-5 kgm ² | 9.5e-6 kgm ² |

flow in the opposite direction. Since, in the dark grey areas in Fig. 2a, power is delivered to the load (output power $T_o\dot{\theta}_o$ is positive), a negative γ results in a positive sun power $T_{mS}\dot{\theta}_S$, but a negative ring power $T_{mR}\dot{\theta}_R$. In this case, the load as well as the ring absorb power which they receive from the sun. In other words, there is an internal power from flow the sun to the ring.

So what is the advantage of this internal power flow? In Verstraten et al. (2018), it is shown that the weakest branch – in this example the ring branch – limits the output torque of a DMA. However, as explained before, a drivetrain can sustain higher output torques when it absorbs power (i.e. in the negative power quadrants) because friction takes over part of the output torque. It can therefore be advantageous to control the ring drivetrain to absorb a (small) amount of negative power: this increases the ring drivetrain's maximum output torque and, consequently, the maximum output torque of the DMA. We thus conclude that the operating range can be enlarged by creating an internal power flow between the sun motor and the ring motor. Although the operating range of kinematically redundant actuators has been analyzed before, this interesting observation has never been reported, because back-driving of motors was prevented by design (Lee and Choi 2012) or simply not considered (Girard and Asada 2015). Nevertheless, we believe that this is an important feature that can potentially be exploited to reduce the need for backdrivable mechanisms or brakes.

4.2 Reflected inertia

The inertia of the drivetrain has an important influence on the energy consumption of an actuator performing a dynamic task.

An overview of the inertias of the drivetrain components in the DMA design and the reference drivetrain is given in Table 3. This table shows that the contribution of the planetary differential to the total inertia in the dual-motor drivetrains is negligible since, in both sun and ring branch, it is attenuated by the gear ratios of the gearbox in that branch. Furthermore, the inertias of the sun and ring branch are an order of magnitude lower than that of the reference drivetrain.

The inertias of the individual drivetrains, of course, do not reveal much about the overall performance of the DMA. This is best represented by the reflected inertia w.r.t. the input (motor side) and the output (load side), which are discussed below.

4.2.1 Inertia reflected to motors The inertia matrix \mathbf{A} , defined in Section 3.2, contains the inertia reflected to the motors:

$$\mathbf{A} = \begin{bmatrix} J_S + \frac{C_S}{n_S^2} \frac{1}{1+\rho C_{PG}} \frac{1}{1+\rho} J_C & \frac{C_S}{n_S n_R} \frac{1}{1+\rho C_{PG}} \frac{\rho}{1+\rho} J_C \\ \frac{C_R}{n_R n_S} \frac{\rho C_{PG}}{1+\rho C_{PG}} \frac{1}{1+\rho} J_C & J_R + \frac{C_R}{n_R^2} \frac{\rho C_{PG}}{1+\rho C_{PG}} \frac{\rho}{1+\rho} J_C \end{bmatrix} \quad (36)$$

The inertia matrix contains coupling terms. Neglecting gearbox losses, the coupling terms are identical and given by

$$J_{coupling} = \frac{1}{n_S n_R} \frac{\rho}{(1+\rho)^2} J_C \quad (37)$$

There are several ways to make the coupling terms disappear: $n_S n_R \rightarrow \infty$, $J_C \rightarrow 0$, $\rho \rightarrow 0$ or $\rho \rightarrow \infty$. Considering that, for a single-stage planetary differential, $1 < \rho$, $\rho \rightarrow 0$ is not realistic. Furthermore, the inertia of the load, if any, will need to be included in J_C . The carrier inertia J_C can therefore not be neglected either. Consequently, the only practical way to reduce the coupling effect is to use high gear reductions n_S , n_R and ρ , although ρ cannot exceed a value of 9 for a single-stage planetary differential. High gear reductions, however, come at the cost of a lower efficiency for the respective planetary gearbox, especially if stages need to be added.

Note that the coupling term (37) has the same form as the “dynamic coupling term” proposed by Rabindran and Tesar (2007) for a DMA design similar to the one presented in this work, but with the ring of the planetary differential as output and the carrier as secondary input. The main difference is the dimensionless ratio ρ , which is defined differently for the two designs.

4.2.2 Inertia reflected to output The total inertia reflected to the output can be defined as

$$J_{DMA,refl}^* = -T_o / \ddot{\theta}_o \quad (38)$$

i.e., the ratio of output torque to output acceleration. An expression for $J_{DMA,refl}^*$ can be obtained by imposing $\mathbf{T}_{2m} = \mathbf{0}$ in Eq. (15) and neglecting all friction terms:

$$\mathbf{0} = \mathbf{A}\dot{\mathbf{x}} + \mathbf{D}T_o \quad (39)$$

By combining Eq. (39) with Eq. (5) and performing some simple mathematical operations, we obtain

$$J_{DMA,refl}^* = (\mathbf{J}\mathbf{A}^{-1}\mathbf{D})^{-1} \quad (40)$$

If gearbox losses are neglected ($C_S = 0$, $C_R = 0$, $C_{PG} = 0$) then $\mathbf{D} = \mathbf{J}^T$, and Eq. (4.2) corresponds to the pseudo kinetic energy matrix defined in Khatib (1987) for kinematically redundant manipulators. In this specific case of a single-output system, $J_{DMA,refl}^*$ is a scalar given by

$$J_{DMA,refl}^* = \frac{(1+\rho)^2}{\frac{1}{J_S n_S^2} + \frac{\rho^2}{J_R n_R^2}} + J_C \quad (41)$$

Note that, if $J_S n_S^2 = 0$ or $J_R n_R^2 = 0$, the reflected inertia $J_{DMA,refl}^*$ will reduce to J_C . In other words, a low inertia in either of both branches will greatly improve the backdrivability of the actuator. Also note that Eq. (41) is independent of the speed ratio γ . This is explained by the fact that, in the derivation of Eq. (41), the influence of the

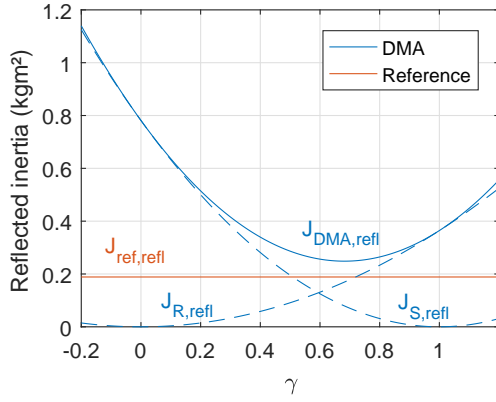


Figure 4. Inertia reflected to load for the DMA ($J_{DMA,refl}(\gamma)$, blue) and the 250W reference motor ($J_{ref,refl}$, red). The contributions of the sun ($J_{S,refl}(\gamma)$) and ring ($J_{R,refl}(\gamma)$) are also indicated with dotted lines. For the DMA, the inertia reflected to the load is a quadratic function of the speed ratio γ .

control input was removed by imposing $\mathbf{T}_{2m} = 0$. Eq. (41) therefore does not provide any insights into how the energetic cost of dynamic motions can be minimized by controlling γ .

To study the influence of the imposed speed ratio γ , we will calculate an alternative expression for the total reflected inertia to the output. We do this by following the approach suggested by Rabindran and Tesar (2008). Here, the reflected inertia is derived by stating that the sum of the system's kinetic energies should be equal to the kinetic energy of the reflected inertia rotating at the output speed. In a lossless system, this can be written as

$$\frac{1}{2} J_{DMA,refl}(\gamma) \cdot \dot{\theta}_o^2 = \frac{1}{2} J_C \dot{\theta}_o^2 + \frac{1}{2} J_S \dot{\theta}_S^2 + \frac{1}{2} J_R \dot{\theta}_R^2 \quad (42)$$

Finding $J_{DMA,refl}(\gamma)$ would require an inversion of Eq. (5). Due to the kinematic redundancy, this is impossible to achieve. As a workaround, we introduced the speed ratio γ , yielding the inverted relationships (9) and (11). This results in the following expression for the reflected inertia:

$$J_{DMA,refl}(\gamma) = J_C + J_{S,refl}(\gamma) + J_{R,refl}(\gamma) \quad (43)$$

with

$$J_{S,refl}(\gamma) = n_S^2 (1 + \rho)^2 (1 - \gamma)^2 J_S \quad (44)$$

$$J_{R,refl}(\gamma) = n_R^2 \frac{(1 + \rho)^2}{\rho^2} \gamma^2 J_R \quad (45)$$

Equation (43) indicates that the reflected inertia of the dual-motor actuator $J_{DMA,refl}(\gamma)$ is a quadratic function of the speed ratio γ . The dependence is visualized in Figure 4 for the dual-motor actuator studied in this work. The minimal reflected inertia $J_{tot,min}$ occurs at

$$\gamma^* = \frac{1}{1 + \frac{J_R n_R^2}{\rho^2 J_S n_S^2}} \quad (46)$$

and is equal to

$$J_{tot,min} = \frac{(1 + \rho)^2}{\frac{1}{J_S n_S^2} + \frac{\rho^2}{J_R n_R^2}} + J_C \quad (47)$$

which is exactly the same expression as Eq. (41). In other words, the reflected inertia $J_{DMA,refl}^* = J_{tot,min}$ corresponds to the minimal value of the γ -dependent reflected inertia $J_{DMA,refl}(\gamma)$.

Interestingly, the value of $J_{tot,min}$ is lower than $J_{DMA,refl}(\gamma = 0)$, where the speed is completely delivered by the ring motor, and $J_{DMA,refl}(\gamma = 1)$, where the speed is completely delivered by the sun drivetrain. This shows that, in terms of reflected inertia, a dual-motor actuator architecture is not bounded by the inertia of its separate branches. Because the kinetic energy of a drivetrain is proportional to the square of the speed, and the output speed of the DMA is divided linearly over both actuators (Eq. (5)), one would expect the dual-motor architecture to be advantageous in applications where high accelerations are required. This will be studied in Section 4.3.

Nevertheless, even the lowest reflected inertia of the DMA $J_{tot,min}$ is still slightly higher than that of the reference motor ($J_{ref,refl}$). A disadvantage of the DMA is that it consists of more rotating components than a conventional actuator. In particular, the ring gear and the couplings required to attach the motors to the differential all add inertia to the actuator. This is, however, not the reason for the higher reflected inertia, since the contribution of these components to the total inertia is negligible compared to the inertias of the sun and ring drivetrains. The real reason is the additional reduction through the planetary differential. Although the inertias of the branches themselves are smaller than that of the reference drivetrain (Table 3), the reduction from the differential causes their inertia, reflected to the output, to be approximately 4 times (sun) and 2 times (ring) higher than that of the reference drivetrain.

Still, it must be noted that this analysis did not consider the efficiency of the actuator, which also has an impact on the reflected inertia. In this regard, it is important to note that the dual-motor actuator was designed to have a higher average efficiency throughout its operating range (Verstraten et al. 2018). The higher efficiency can compensate somewhat for the increased reflected inertia. Furthermore, the reflected inertia was not considered in the design phase. By doing so, it might be possible to conceive a design with lower reflected inertia, without compromising on efficiency.

4.3 Maximum acceleration

So far, we have established that the DMA has a slightly larger operating range, but a higher reflected inertia. We will now discuss how this translates to the maximum achievable output acceleration.

A common metric to assess the acceleration capability is the ratio between the maximum torque T_{max} and the rotor inertia J_m . An analysis similar to the one presented in Haddadin et al. (2012) shows that this metric scales with the motor's length l_m and its radius r_m as

$$\frac{T_{max}}{J_m} \sim l_m^0 r_m^{-3/2} \quad (48)$$

This relationship is in line with catalog data, which exhibits a scaling of $T_{max}/J_m \sim r_m^{-1.6}$ (Wensing et al. 2017). A motor's acceleration capability is thus proportional to its length and decreases with its radius according to $r_m^{-3/2}$. In

other words, smaller motors can deliver relatively higher accelerations. This appears to be a favorable situation for the DMA where, in essence, we replaced a large motor with two smaller ones. However, the DMA also links the accelerations and torques of the output to those of the motors, which complicates the discussion. Consequently, a more detailed analysis is required to assess whether a DMA really can really reach higher accelerations.

In accordance with Eq. (5), the maximum output acceleration is simply the sum of the maximum accelerations of the sun and ring branch:

$$\ddot{\theta}_{max} = \mathbf{J} \begin{bmatrix} \ddot{\theta}_{Smax} \\ \ddot{\theta}_{Rmax} \end{bmatrix} \quad (49)$$

In order to relate the maximum acceleration to the design, we simplify the motor torque (15) by neglecting friction:

$$\mathbf{T}_{2m} = \mathbf{A}\dot{\mathbf{x}} + \mathbf{D}T_o \quad (50)$$

There are two contributions to the motor torque that must be taken into account. The first part is related to the accelerations of the motors, which is strongly influenced by γ . The second part is related to the desired output torque T_o . This torque is divided over both motors according to Eq. (15), and consumes current from both motors. The distribution over the motors is determined by the design (parameter ρ) and, in contrast to the other term, cannot be influenced by the speed ratio γ – except indirectly, through manipulation of the speed-related friction terms.

The maximum acceleration for a specific static output torque is achieved when both motor torques saturate. Defining the vector of saturated motor torques,

$$\mathbf{T}_{2max} = \begin{bmatrix} T_{Smax} \\ T_{Rmax} \end{bmatrix} = \begin{bmatrix} k_{TS} I_{Smax,peak} \\ k_{TR} I_{Rmax,peak} \end{bmatrix} \quad (51)$$

Eq. (50) can be rewritten as

$$\mathbf{A}^{-1}(\mathbf{T}_{2max} - \mathbf{D}T_o) = \begin{bmatrix} \ddot{\theta}_{Smax} \\ \ddot{\theta}_{Rmax} \end{bmatrix} \quad (52)$$

Left multiplication with \mathbf{J} , defined in Eq. (6), gives

$$\mathbf{J}\mathbf{A}^{-1}(\mathbf{T}_{2max} - \mathbf{D}T_o) = \ddot{\theta}_{max} \quad (53)$$

This equation defines the maximum acceleration $\ddot{\theta}_{max}$ for a specific output torque T_o . If we neglect the efficiencies C_{PG} , C_S and C_R and assume that both motors are identical ($T_{Smax} = T_{Rmax} \triangleq T_{max}$ and $J_S = J_R \triangleq J_m$), we find the maximum acceleration

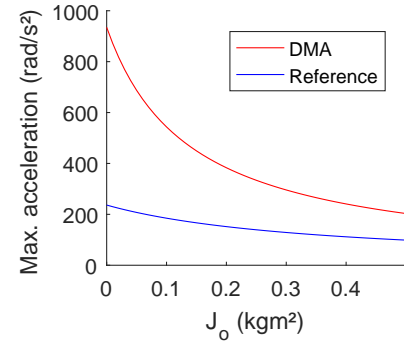
$$\ddot{\theta}_{max}(T_o) = \frac{\frac{1}{1+\rho} \left(\frac{1}{n_S} + \frac{\rho}{n_R} \right) T_{max} - \frac{1}{(1+\rho)^2} \left(\frac{1}{n_S^2} + \frac{\rho^2}{n_R^2} \right) T_o}{J_m + \left(\frac{1}{n_S^2} \frac{1}{(1+\rho)^2} + \frac{1}{n_R^2} \frac{\rho^2}{(1+\rho)^2} \right) J_o} \quad (54)$$

where we replaced the carrier inertia J_C with J_o , the combined inertia of the carrier and load:

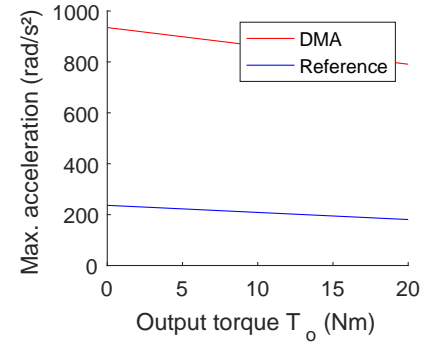
$$J_o = J_C + J_{load} \quad (55)$$

Compare to a regular DC motor with gear reducer:

$$\ddot{\theta}_{max}(T_o) = \frac{\frac{1}{n} T_{max} - \frac{1}{n^2} T_o}{J_m + \frac{J_o}{n^2}} \quad (56)$$



(a)



(b)

Figure 5. Influence on the maximum acceleration of (a) load inertia J_o and (b) static torque T_o . In Fig. (a), $T_o = 0$ Nm, and in Fig. (b), $J_o = 0$ kgm². There is an inverse quadratic relationship between $\ddot{\theta}_{max}$ and J_o , and an inverse linear relationship between $\ddot{\theta}_{max}$ and T_o . The DMA can achieve much higher accelerations than the reference actuator at low loads. However, the output torque and, especially, the load inertia have a much stronger effect on the DMA. For high values of J_o , the maximum achievable acceleration of the DMA approaches that of the reference actuator, and will eventually drop below it.

In Eq. (54), it is not the sum of actuator inertias $J_S + J_R \approx 2J_m$ but the inertia of a single motor (J_m) that appears. This implies that the maximum acceleration scales favorably with the inertias of the DMA drivetrains. On the other hand, if

$$n = \frac{1}{1+\rho} \left(\frac{1}{n_S} + \frac{\rho}{n_R} \right) \quad (57)$$

then

$$n^2 > \frac{1}{(1+\rho)^2} \left(\frac{1}{n_S^2} + \frac{\rho^2}{n_R^2} \right) \quad (58)$$

The static output torque and load inertia are thus reduced more strongly by the conventional solution of a motor with gear reducer. This means that, if the DMA and the conventional actuator are designed to deliver the same static torque output, the conventional actuator will perform better dynamically at high output torques or with high inertial loads. However, as demonstrated in Table 3, the inertia J_m of the DMA's motors can be made smaller than that of a single drivetrain. As a consequence, the DMA starts off with a higher acceleration capability, which nonetheless declines more rapidly with increasing J_o and T_o than that of the reference drivetrain. This is visualized in Fig. 5.

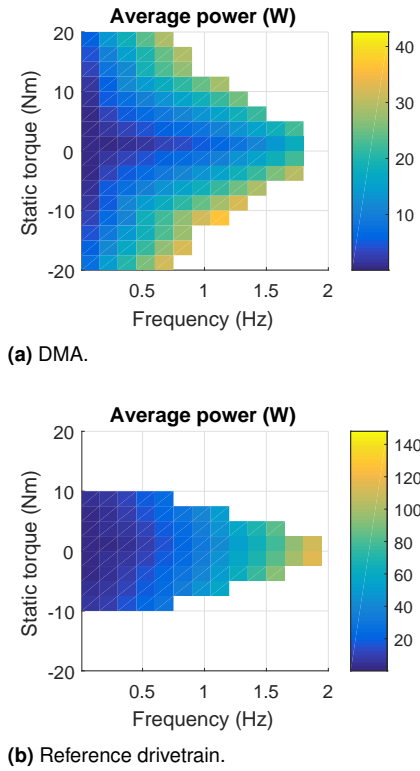


Figure 6. Average electrical power per cycle required by (a) the dual-motor actuator and (b) the reference motor to complete the cyclic task given by Eqs. (59) and (60). The speeds are calculated with optimal control, as specified in Section 3.5. The dual-motor actuator maintains more of its acceleration capability at high static loads. Furthermore, its energy consumption is generally lower than that of the single-motor solution.

4.4 Energy efficiency comparison

In order to evaluate the energy efficiency of the actuator, we calculate the electrical energy consumption in a task where the actuator applies a sinusoidal speed to a variable load. The trajectory is given by

$$\dot{\theta}_{imp} = A_0 \omega \sin(\omega t) \quad (59)$$

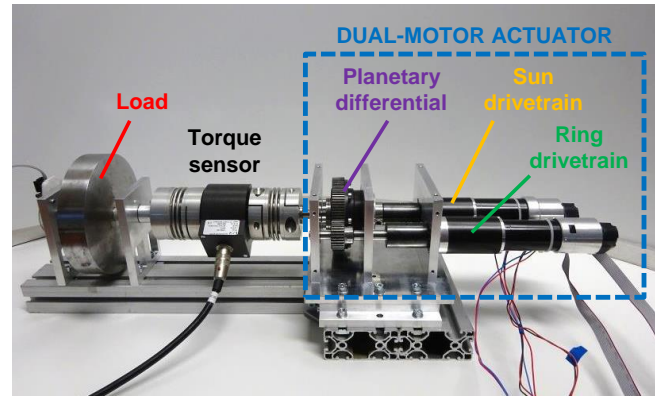
with fixed amplitude $A_0 = 60^\circ$ and variable frequency ω . The variable load consists of a variable static torque T_o and a constant inertial load ($J_{load} = 11.7 \text{ gm}^2$):

$$T_{load} = T_o + J_{load} A_0 \omega^2 \cos(\omega t) \quad (60)$$

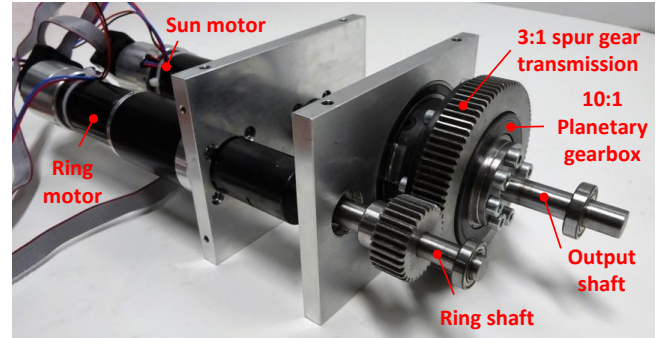
Based on the inertia matching principle (Pasch and Seering 1984), the reference drivetrain design would be ideal for an inertial load of $J_{load} = 0.17 \text{ kgm}^2$. The actual inertial load is more than ten times lower to reflect the problem of performing dynamic motions with drivetrains designed for high torques, explained in the introduction of this article.

By varying the static torque T_o and the frequency ω , we can test the actuator's dynamic capabilities for different static loads. The results are shown in Fig. 6.

In the absence of a static load, the reference drivetrain is capable of reaching slightly higher frequencies than the DMA, but the difference is rather small. Conversely, the DMA is much more capable of dealing with static torques. In accordance with the results from Section 4.1, the reference drivetrain can only deliver torques of up to 10 Nm at



(a) Test setup with inertial load.



(b) Close-up view of the DMA.

Figure 7. Experimental test setup.

low frequencies, whereas the DMA can reach more than 20 Nm. What also sets both actuators apart is their energy consumption, presented in Fig. 6 as the average electrical power over a cycle. At low frequencies, the electrical energy consumption is quite similar, but the difference increases fast with increasing frequency. At frequencies approaching 2 Hz, the average power of the reference drivetrain easily exceeds 100 W, while the average power of the DMA is only around 30 W. In conclusion, these calculations demonstrate that the better quasi-static efficiency of the DMA outweighs the slight increase in reflected inertia.

5 Experimental results

In order to validate the results, an experimental test setup was built. In this setup, depicted in Fig. 7a, a dual-motor actuator (close-up in Fig. 7b) is coupled to a flywheel, which acts as the load. The flywheel has an inertia of $J_{load} = 11.7 \text{ gm}^2$, the same as in Section 4.4. The DMA is built using only off-the-shelf components, and matches the one studied in Section 4 (parameters in Tables 1 and 2). It consists of a planetary differential, constructed out of a 10:1 Neugart PLFE 064 planetary gearbox with an ordinary spur gear attached to the ring. The sun gear is driven by a 150W Maxon RE40 DC motor with a Maxon GP42C planetary gear reducer of ratio 15:1, and the ring gear by a 90W Maxon RE35 DC motor with a 43:1 reduction provided by a Maxon GP42C planetary gearbox. The ring drivetrain is coupled to the ring by means of a 3:1 spur gear transmission, bringing the total reduction of the ring branch to 129:1. Both motors are equipped with a Maxon AB24 holding brake (24V, 0.4Nm) which adds an inertia of 1 gcm^2 to the motor.

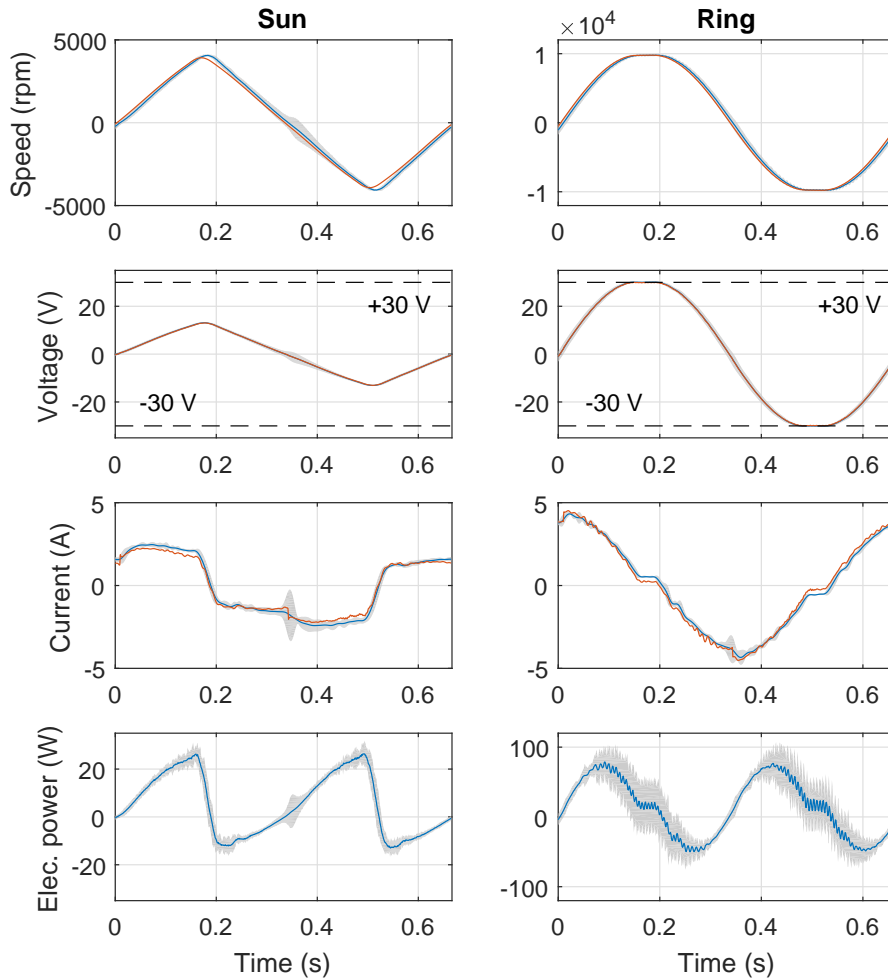


Figure 8. Modeled (red) and measured (blue) speeds, voltages, currents and electrical powers in the ring and sun branch, for a sinusoidal output speed with a frequency of 1.5 Hz. The measured values are averages over at least ten cycles. The 3σ confidence interval is shown as a grey fill.

An ETH Messtechnik DRBK-50 torque sensor is mounted between the actuator and the load. Finally, a US Digital E6 encoder (2000 CPT) measures the output position. The motor positions and speeds are retrieved from Maxon HEDL 5540 encoders (500 CPT) mounted on the motor shafts. The signals from these encoders also serve as feedback for the speed control, which is performed by a Maxon EPOS3 controller (sun motor) and a Maxon MAXPOS 50/5 controller (ring motor), using the built-in profile velocity mode. The electrical power measurement is obtained by multiplying the motor voltage and current. Voltage is sensed with custom-made differential amplifiers, while the current is retrieved directly from the EPOS3 and MAXPOS units.

A sinusoidal speed is imposed at the output, according to the specifications in Section 4.4. Imposed frequencies are 0.25, 0.5, 1 and 1.5 Hz. The imposed input speeds are obtained from optimal control, as explained in Section 3.5.

5.1 High-frequency measurement

We first present a high-frequency measurement in order to gain a better understanding of how the DMA works, and to demonstrate the validity of the model. Figure 8 shows

the speed, currents and electrical power consumption for the measurement at 1.5 Hz.

5.1.1 Speed distribution The speed trajectories of the sun and ring are roughly sinusoidal, their frequency in line with that of the imposed trajectory. Between 0.14–0.2 s and 0.48–0.53 s, the ring speed is capped at approximately 10 000 rpm. This is due to saturation of the voltage, which was limited to 30 V (see Section 3.4). To ensure that the correct output speed is still reached, the sun delivers a slightly higher speed during these time intervals, giving its speed profile a sawtooth-like appearance.

Higher-frequency components are avoided in order to prevent additional accelerations, which are the cause of most of the torque delivered by the motors. This means that the speed ratio γ should roughly be constant throughout most of the cycle. Indeed, in Fig. 9, which shows the (imposed) speed ratio over a range of cycles with different frequencies, we observe that γ tends to stay close to a single value for most of the cycle. For frequencies of 0.5 Hz and below, $\gamma = 1$ at all times, meaning that the sun is held still and all speed is being delivered by the ring branch – the most efficient branch in the design. Because, at this low frequency, the dynamics can

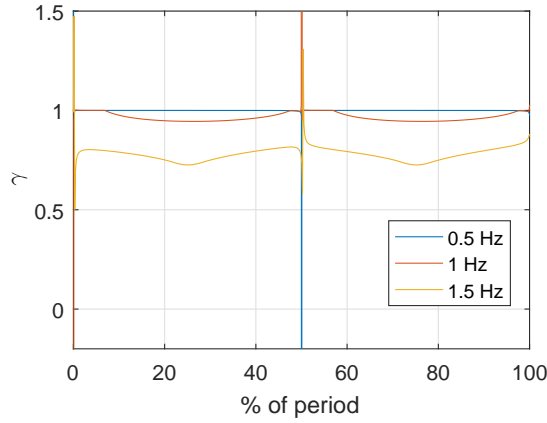


Figure 9. Imposed speed ratio γ over a range of sinusoidal cycles with different frequencies. At low frequencies, only the ring branch – the most efficient branch – is used, corresponding to a speed ratio of $\gamma = 1$. When the frequency is increased, γ takes on an average value between 0 and 1 in order to reduce the reflected inertia. Upon velocity reversals (0%, 50% and 100% of cycle), γ can take on values above one or below zero to smoothen the acceleration profiles of the individual motors.

be neglected, this result can be found by tracing the required combinations of output torque and speed on the map with the optimal speed ratio (Fig. 3). With a peak output torque of 0.12 Nm and a maximum output speed of 30 rpm for the 0.5 Hz measurement, it is easy to see that the speed ratio $\gamma = 1$ indeed corresponds to the optimal speed ratio according to the map. At higher frequencies, the average value of γ decreases towards $\gamma^* = 0.68$, the value that minimizes the reflected inertia $J_{DMA,refl}(\gamma)$, as discussed in Section 4.2. We can therefore conclude that, in highly dynamic motions, the decrease of individual motor speeds and accelerations dominates the choice of the optimal speed distribution.

5.1.2 Current Many of the conclusions in this work are derived from the dynamic model presented in Section 3. The validity of the model is proven by the excellent agreement between the measured currents (blue) and the currents estimated from Eqs. (15)-(21) (red). The currents in both drivetrains are dominated by the inertial torque of the respective drivetrain, and therefore follow their acceleration pattern.

5.1.3 Electrical power and power flows Fig. 8 shows that the peak electrical power in the ring branch is approximately three times higher than that of the sun branch. But how much of this power makes its way to the load, and how much is lost as heat? To gain a better understanding of the power consumption, we present four important contributions to the electrical power in Fig. 10: the power related to the inertia of the load ($J_{load}\ddot{\theta}_o\dot{\theta}_o$), the power related to the inertia of the drivetrain ($J_\lambda\ddot{\theta}_\lambda\dot{\theta}_\lambda$), the Joule losses ($R_\lambda I_\lambda^2$) and the friction losses, which include the power lost through viscous and Coulomb friction, as well as the gearbox losses.

The power flow related to the load is almost negligible compared to the power flows related to the inertia of the branches. In both branches, most of the input power is used to move the inertia of the drivetrain itself. This is a result of using a drivetrain designed for high torques to perform dynamic motion. Such drivetrains are composed of

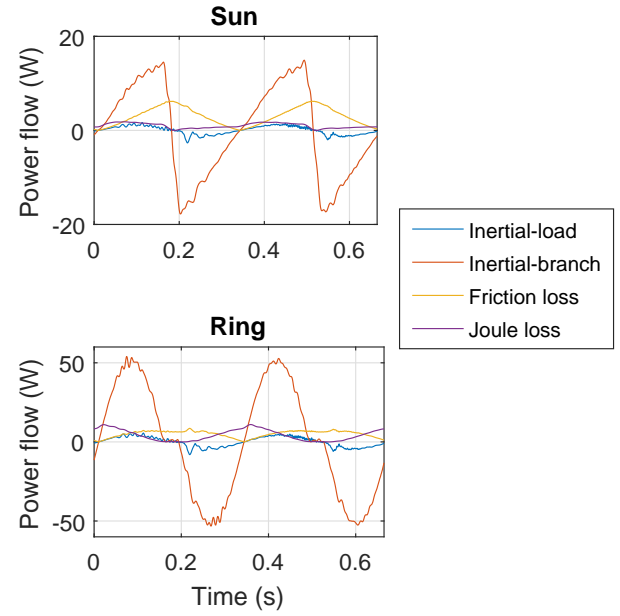


Figure 10. Power flows for a sinusoidal oscillation at 1.5 Hz, averaged over ten cycles. The power flows were estimated from the position and current measurements.

high torque motors and/or high gear reductions, leading to drivetrain inertia which is much higher than the inertia of the robot's links. When the payload is removed, most power will move back and forth from the motor to the drivetrain inertia.

Inertia acts as an energy buffer, and therefore, the net energy consumption of these power flows, however big they are, is zero. They do, however, have an influence on the required motor torque and, consequently, on the Joule losses. These are much higher in the ring branch, where the acceleration is the highest. The winding resistance in the ring branch ($R_R = 583 \text{ m}\Omega$) is also almost twice as high as that of the sun branch ($R_S = 299 \text{ m}\Omega$).

The other source of losses is friction. Friction losses are related to the speed of the drivetrains, and therefore are not affected by the drivetrain inertia. The losses are similar in the sun and ring branch, but their contribution relative to the total power flow is clearly higher in the sun branch, which has the highest friction coefficients.

5.2 Energetic comparison

The measurements also allow for a direct comparison with the simulated energy consumption in Section 4.4. The calculated average power over a cycle is shown in Figure 11 and compared to the measurements on the setup. The measured values are slightly higher than the predicted values, indicating that there are still some unmodeled losses in the system. Nevertheless, the quantitative behavior is similar. Figure 11 also provides a good visualization of the difference between the reference drivetrain (red) and the DMA (blue). The energy consumption of the reference drivetrain rises much more quickly than that of the DMA. At a frequency of 1.5 Hz, the DMA only consumes 18 % of the energy consumed by the reference drivetrain.

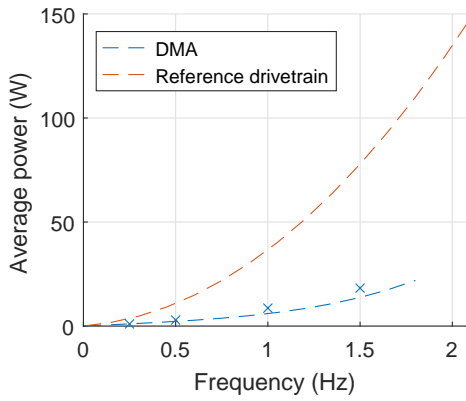


Figure 11. Average power consumption in case of a purely inertial load of 12 gm². The estimated power consumption obtained from the optimization is denoted by the dashed lines, while experimentally obtained powers are denoted by crosses. For reference, the estimated power consumption of the reference drivetrain is plotted in red. There is a good match between the experiments and the estimations.

6 Discussion In this section, we briefly summarize and discuss the main advantages and disadvantages of the DMA design, based on the findings presented in this work.

6.1 Extended operating range

In Section 4.1, we made the interesting observation that the DMA was *capable of providing high torques at low speeds in the positive power quadrants*, whereas the single-motor alternative was not. This was achieved by exploiting internal power flows. If the power flow in the most loaded branch is reversed, friction can be used to absorb a part of the output power, lowering the torque requirement from the motor. This is a very important finding, since internal power flows are generally considered to have an adverse effect on the actuator's efficiency, and therefore avoided. This explains why, in previous analyses, the benefit of internal power flows in terms of operating range was not discovered. We do, however, consider the extended operating range as a strong potential advantage, even if it comes at a slightly higher energetic cost. The extended operating range may, for example, reduce the need for brakes or non-backdrivable mechanisms which increase the volume, weight and mechanical complexity of the actuator.

6.2 Increased acceleration capability and energy efficiency

The main goal of the study was to gain insight in how the DMA performs in dynamic tasks. In Section 4.2, we concluded that the ratio between the ring speed and output speed, characterized by the variable γ , can be chosen in such a way that the inertia of the actuator, reflected to the output, is smaller than that of its composing drivetrains. Nevertheless, we also found the minimal reflected inertia of our DMA design to be slightly higher than that of a single-motor alternative. This does not have to be a disadvantage in terms of dynamic performance, though. In Section 4.3,

the maximum acceleration of the DMA was shown to be higher than the single-motor reference drivetrain, although the advantage declines with the inertia of the load. The DMA, thanks to its extended operating range, was also able to provide higher accelerations when a static torque was added to the load. Furthermore, its *energy consumption is considerably lower than that of its single-motor equivalent*. This was evidenced by the calculations in Section 4.4 and the experimental results in Section 5.2.

6.3 Flexibility towards conflicting torque-speed requirements

The optimal speed distribution γ depends strongly on the required output torque, speed and acceleration. If the accelerations are low, most power will go through the branch with the least amount of friction. For higher accelerations, the optimal speed ratio tends to move towards the speed ratio that minimizes the reflected inertia. *In other words, the speed ratio γ of the DMA can be tuned to meet the conflicting torque-speed requirements of loaded and unloaded phases in robotic tasks.* The results from Section 5.1.1 suggest that this adaptation should be performed relatively slowly with respect to the motion. In all our trials with sinusoidal output speeds, γ remained fairly constant, indicating that rapid changes in γ should be avoided because of the additional energetic costs that would result from the high accelerations related to the high-frequency motion.

6.4 Trade-offs and further opportunities

Kinematically redundant actuators also have an obvious disadvantage: the redundant drivetrains lead to a higher total number of components. This gives rise to increased investment costs and entails additional complexity in terms of design, assembly and control. Intuitively, one would also expect the volume and weight of the DMA to be larger than that of a single-motor alternative. This is, however, not necessarily true, since a kinematically redundant design may be composed of smaller and lighter motors in combination with smaller, more efficient gearboxes. The results in [Verstraten et al. \(2018\)](#), for example, indicate that a DMA design can actually be made lighter than a single-motor alternative having the same operating range, provided that its composing drivetrains are selected in a smart way. With integrated designs, where the motors and the planetary differential are combined in a single housing ([Girard and Asada 2015](#)), the actuator's volume and weight can be further reduced. Even greater advantages may be achieved by adding non-backdrivable elements to the design, as they allow shaping the working range of the actuator to fit the application more closely. However, as discussed in the introduction of Section 4, the reduction in size and weight of motors and gearboxes must be assessed against the volume, weight and complexity added by the non-backdrivable mechanisms. This work, where the optimal usage of a simple DMA without brakes was studied, can serve as a baseline for comparison.

7 Conclusion

In this work, we explored the potential of kinematically redundant actuators by studying its most common embodiment: two electric motors coupled by a planetary differential. To assess its qualities, this actuator, which we named “Dual-Motor Actuator” (DMA), was evaluated against a single-motor alternative capable of spanning roughly the same operating range. Our results indicate that a DMA can, indeed, be used as an energy-efficient alternative to a classic drivetrain consisting of a motor with speed reducer. Its capability of providing higher torques at low speeds, combined with its ability to divide the acceleration over two motors, makes it a very suitable solution for applications which require a wide range of torques, speeds and accelerations.

Acknowledgements

Tom Verstraten is a PhD Fellow of the Research Foundation Flanders - Fonds voor Wetenschappelijk Onderzoek (FWO). David Rodriguez-Cianca is an SB Fellow of the same organisation. Part of this work was funded by the European Commission starting grant SPEAR (no. 337596).

References

- Aló R, Bottiglione F and Mantriota G (2015) An innovative design of artificial knee joint actuator with energy recovery capabilities. *Journal of Mechanisms and Robotics* 8(1): 011009–011009. DOI:10.1115/1.4030056.
- Babin V, Gosselin C and Allan JF (2014) A dual-motor robot joint mechanism with epicyclic gear train. In: *Intelligent Robots and Systems (IROS 2014), 2014 IEEE/RSJ International Conference on*. pp. 472–477. DOI:10.1109/IROS.2014.6942601.
- Belter JT and Dollar AM (2014) A passively adaptive rotary-to-linear continuously variable transmission. *IEEE Transactions on Robotics* 30(5): 1148–1160. DOI:10.1109/TRO.2014.2333096.
- Biegler L and Zavala V (2009) Large-scale nonlinear programming using ipopt: An integrating framework for enterprise-wide dynamic optimization. *Computers & Chemical Engineering* 33(3): 575 – 582. DOI:http://dx.doi.org/10.1016/j.compchemeng.2008.08.006. Selected Papers from the 17th European Symposium on Computer Aided Process Engineering held in Bucharest, Romania, May 2007.
- Brown W and Ulsoy A (2013) A maneuver based design of a passive-assist device for augmenting active joints. *Journal of Mechanisms and Robotics* 5(3): 031003. DOI:10.1115/1.4024237.
- Carbone G, Mangialardi L and Mantriota G (2001) Fuel consumption of a mid class vehicle with infinitely variable transmission. In: *SAE Technical Paper*. SAE International. DOI:10.4271/2001-01-3692.
- Dresscher D, de Vries TJA and Stramigioli S (2015) Inertia-driven controlled passive actuation. In: *ASME 2015 Dynamic Systems and Control Conference*, 57267. pp. V003T45A002–. DOI: 10.1115/DSCC2015-9786.
- Dresscher D, Naves M, de Vries T, Buijze M and Stramigioli S (2017) Power split based dual hemispherical continuously variable transmission. *Actuators* 6(2): 15. DOI:10.3390/act6020015.
- Everarts C, Dehez B and Ronsse R (2015) Novel infinitely variable transmission allowing efficient transmission ratio variations at rest. In: *Intelligent Robots and Systems (IROS), 2015 IEEE/RSJ International Conference on*. pp. 5844–5849. DOI:10.1109/IROS.2015.7354207.
- Fauteux P, Lauria M, Heintz B and Michaud F (2010) Dual-differential rheological actuator for high-performance physical robotic interaction. *IEEE Transactions on Robotics* 26(4): 607–618. DOI:10.1109/TRO.2010.2052880.
- Fumagalli M, Stramigioli S and Carloni R (2014) Analysis of a variable stiffness differential drive (VSDD). In: *2014 IEEE International Conference on Robotics and Automation (ICRA)*. pp. 2406–2411. DOI:10.1109/ICRA.2014.6907193.
- Gao P, Ren A and Zong W (2016) Study on a variable stiffness actuation with differential drives. In: *2016 IEEE International Conference on Cyber Technology in Automation, Control, and Intelligent Systems (CYBER)*. pp. 249–254. DOI:10.1109/CYBER.2016.7574831.
- Girard A and Asada HH (2015) A two-speed actuator for robotics with fast seamless gear shifting. In: *Intelligent Robots and Systems (IROS), 2015 IEEE/RSJ International Conference on*. pp. 4704–4711. DOI:10.1109/IROS.2015.7354047.
- Girard A and Asada HH (2016) A practical optimal control approach for two-speed actuators. In: *2016 IEEE International Conference on Robotics and Automation (ICRA)*. pp. 4572–4577. DOI:10.1109/ICRA.2016.7487658.
- Girard A and Asada HH (2017) Leveraging natural load dynamics with variable gear-ratio actuators. *IEEE Robotics and Automation Letters* 2(2): 741–748. DOI:10.1109/LRA.2017.2651946.
- Grimmer M, Eslamy M and Seyfarth A (2014) Energetic and peak power advantages of series elastic actuators in an actuated prosthetic leg for walking and running. *Actuators* 3(1): 1. DOI: 10.3390/act3010001.
- Groothuis SS, Carloni R and Stramigioli S (2016) Single motor-variable stiffness actuator using bistable switching mechanisms for independent motion and stiffness control. In: *2016 IEEE International Conference on Advanced Intelligent Mechatronics (AIM)*. pp. 234–239. DOI:10.1109/AIM.2016.7576772.
- Haddadin S, Mansfield N and Albu-Schaffer A (2012) Rigid vs. elastic actuation: Requirements & performance. In: *Intelligent Robots and Systems (IROS), 2012 IEEE/RSJ International Conference on*. pp. 5097–5104. DOI:10.1109/IROS.2012.6386227.
- Hitt JK, Sugar TG, Holgate M and Bellman R (2010) An active foot-ankle prosthesis with biomechanical energy regeneration. *Journal of Medical Devices* 4(1): 011003. DOI:10.1115/1.4001139.
- Hu JS, Wu CH, Tsai YJ and Kuo CH (2015) Study on the characteristics of a homemade differential-velocity-type compliant joint for robotic manipulators. *Advances in Mechanical Engineering* 7(9): 1687814015603668. DOI:10.1177/1687814015603668.
- Kembaum AS, Kitchell M and Crittenden M (2017) An ultra-compact infinitely variable transmission for robotics. In: *2017 IEEE International Conference on Robotics and Automation (ICRA)*. pp. 1800–1807. DOI:10.1109/ICRA.2017.7989212.
- Khatib O (1987) A unified approach for motion and force control of robot manipulators: The operational space formulation. *IEEE*

- Journal on Robotics and Automation* 3(1): 43–53. DOI:10.1109/JRA.1987.1087068.
- Kim BS, Park JJ and Song JB (2007) Improved manipulation efficiency using a serial-type dual actuator unit. In: *Control, Automation and Systems, 2007. ICCAS '07. International Conference on*. pp. 30–35. DOI:10.1109/ICCAS.2007.4406874.
- Kim BS, Song JB and Park JJ (2010) A serial-type dual actuator unit with planetary gear train: Basic design and applications. *IEEE/ASME Transactions on Mechatronics* 15(1): 108–116. DOI:10.1109/TMECH.2009.2019639.
- Lee H and Choi Y (2012) A new actuator system using dual-motors and a planetary gear. *IEEE/ASME Transactions on Mechatronics* 17(1): 192–197. DOI:10.1109/TMECH.2011.2165221.
- Lenzi T, Cempini M, Hargrove LJ and Kuiken TA (2017) Actively variable transmission for robotic knee prostheses. In: *2017 IEEE International Conference on Robotics and Automation (ICRA)*. pp. 6665–6671. DOI:10.1109/ICRA.2017.7989787.
- Mangialardi L and Mantriota G (1994) Automatically regulated C.V.T. in wind power systems. *Renewable Energy* 4(3): 299 – 310. DOI:http://dx.doi.org/10.1016/0960-1481(94)90033-7.
- Mathijssen G, Furnémont R, Verstraten T, Brackx B, Premec J, Jiménez R, Lefeber D and Vanderborght B (2016) +SPEA introduction: Drastic actuator energy requirement reduction by symbiosis of parallel motors, springs and locking mechanisms. In: *2016 IEEE International Conference on Robotics and Automation (ICRA)*. pp. 676–681. DOI:10.1109/ICRA.2016.7487193.
- Mohammed A, Schmidt B and Wang L (2016) Energy-efficient robot configuration for assembly. *Journal of Manufacturing Science and Engineering* 139(5): 051007–051007–7. DOI:10.1115/1.4034935.
- Mooney L and Herr H (2013) Continuously-variable series-elastic actuator. In: *IEEE International Conference on Rehabilitation Robotics*.
- Morrell JB and Salisbury JK (1998) Parallel-coupled micro-macro actuators. *The International Journal of Robotics Research* 17(7): 773–791. DOI:10.1177/027836499801700707.
- Müller HW (1982) *Epicyclic drive trains: Analysis, synthesis, and applications*. Wayne State University Press.
- Nagai K, Dake Y, Shiigi Y, Loureiro RCV and Harwin WS (2010) Design of redundant drive joints with double actuation using springs in the second actuator to avoid excessive active torques. In: *2010 IEEE International Conference on Robotics and Automation*. pp. 805–812. DOI:10.1109/ROBOT.2010.5509902.
- Nagai K, Shiigi Y, Ikegami Y, Loureiro RCV and Harwin WS (2009) Impedance control of redundant drive joints with double actuation. In: *2009 IEEE International Conference on Robotics and Automation*. pp. 1528–1534. DOI:10.1109/ROBOT.2009.5152472.
- Olsson H, Åström K, de Wit CC, Gäfvert M and Lischinsky P (1998) Friction models and friction compensation. *European Journal of Control* 4(3): 176 – 195. DOI:http://dx.doi.org/10.1016/S0947-3580(98)70113-X.
- Ontañón Ruiz J, Daniel RW and McÄree PR (1998) On the use of differential drives for overcoming transmission nonlinearities. *Journal of Robotic Systems* 15(11): 641–660. DOI:10.1002/(SICI)1097-4563(199811)15:11<641::AID-ROB3>3.0.CO;2-T.
- Paryanto, Brossog M, Bornschlegl M and Franke J (2015) Reducing the energy consumption of industrial robots in manufacturing systems. *The International Journal of Advanced Manufacturing Technology* 78(5): 1315–1328. DOI:10.1007/s00170-014-6737-z.
- Pasch KA and Seering W (1984) On the drive systems for high-performance machines. *Journal of Mechanical Design* 106(1): 102–108. DOI:10.1115/1.3258545.
- Patterson MA and Rao AV (2014) GPOPS-II: A MATLAB software for solving multiple-phase optimal control problems using hp-adaptive gaussian quadrature collocation methods and sparse nonlinear programming. *ACM Trans. Math. Softw.* 41(1): 1:1–1:37. DOI:10.1145/2558904.
- Plooij M and Wisse M (2012) A novel spring mechanism to reduce energy consumption of robotic arms. In: *Intelligent Robots and Systems (IROS), 2012 IEEE/RSJ International Conference on*. pp. 2901–2908. DOI:10.1109/IROS.2012.6385488.
- Rabindran D and Tesar D (2007) Study of the dynamic coupling term (μ) in parallel force/velocity actuated systems. In: *2007 IEEE International Conference on Automation Science and Engineering*. pp. 418–423. DOI:10.1109/COASE.2007.4341821.
- Rabindran D and Tesar D (2008) Parametric design and power-flow analysis of parallel force/velocity actuators. *Journal of Mechanisms and Robotics* 1(1): 011007–011007–10. DOI:10.1115/1.2959100.
- Rabindran D and Tesar D (2014) A differential-based dual actuator for a safe robot joint: Theory and experiments. In: *2014 World Automation Congress (WAC)*. pp. 142–147. DOI:10.1109/WAC.2014.6935734.
- Remy CD, Buffinton K and Siegwart R (2012) Comparison of cost functions for electrically driven running robots. In: *2012 IEEE International Conference on Robotics and Automation*. pp. 2343–2350. DOI:10.1109/ICRA.2012.6224960.
- Roozing W, Li Z, Caldwell DG and Tsagarakis NG (2016) Design optimisation and control of compliant actuation arrangements in articulated robots for improved energy efficiency. *IEEE Robotics and Automation Letters* 1(2): 1110–1117. DOI:10.1109/LRA.2016.2521926.
- Seok S, Wang A, Chuah MY, Otten D, Lang J and Kim S (2013) Design principles for highly efficient quadrupeds and implementation on the MIT Cheetah robot. In: *Robotics and Automation (ICRA), 2013 IEEE International Conference on*. pp. 3307–3312. DOI:10.1109/ICRA.2013.6631038.
- Srivastava N and Haque I (2009) A review on belt and chain continuously variable transmissions (CVT): Dynamics and control. *Mechanism and Machine Theory* 44(1): 19 – 41. DOI:http://dx.doi.org/10.1016/j.mechmachtheory.2008.06.007.
- Stramigioli S, van Oort G and Dertien E (2008) A concept for a new energy efficient actuator. In: *Advanced Intelligent Mechatronics, 2008. AIM 2008. IEEE/ASME International Conference on*. pp. 671–675. DOI:10.1109/AIM.2008.4601740.
- Sugar TG and Holgate M (2013) Compliant mechanisms for robotic ankles. In: *ASME 2013 International Design Engineering Technical Conferences and Computers and Information in Engineering Conference*. American Society of Mechanical Engineers, pp. V06AT07A002–V06AT07A002. DOI:10.1115/DETC2013-12167.

- Tagliamonte NL, Sergi F, Accoto D, Carpino G and Guglielmelli E (2012) Double actuation architectures for rendering variable impedance in compliant robots: A review. *Mechatronics* 22(8): 1187 – 1203. DOI:<http://dx.doi.org/10.1016/j.mechatronics.2012.09.011>.
- Tagliamonte NL, Sergi F, Carpino G, Accoto D and Guglielmelli E (2010) Design of a variable impedance differential actuator for wearable robotics applications. In: *2010 IEEE/RSJ International Conference on Intelligent Robots and Systems*. pp. 2639–2644. DOI:10.1109/IROS.2010.5649982.
- Tucker M and Fite K (2010) Mechanical damping with electrical regeneration for a powered transfemoral prosthesis. In: *Advanced Intelligent Mechatronics (AIM), 2010 IEEE/ASME International Conference on*. pp. 13–18. DOI:10.1109/AIM.2010.5695828.
- Uemura M and Kawamura S (2009) Resonance-based motion control method for multi-joint robot through combining stiffness adaptation and iterative learning control. In: *Robotics and Automation, 2009. ICRA '09. IEEE International Conference on*. pp. 1543–1548. DOI:10.1109/ROBOT.2009.5152717.
- Vanderborght B, Albu-Schaeffer A, Bicchi A, Burdet E, Caldwell D, Carloni R, Catalano M, Eiberger O, Friedl W, Ganesh G, Garabini M, Grebenstein M, Grioli G, Haddadin S, Hoppner H, Jafari A, Laffranchi M, Lefeber D, Petit F, Stramigioli S, Tsagarakis N, Van Damme M, Van Ham R, Visser L and Wolf S (2013) Variable impedance actuators: A review. *Robotics and Autonomous Systems* 61(12): 1601 – 1614. DOI:<http://dx.doi.org/10.1016/j.robot.2013.06.009>.
- Verstraten T, Furnémont R, Lopez-Garcia P, Rodriguez-Cianca D, Cao HL, Vanderborght B and Lefeber D (2018) Modeling and design of an energy-efficient dual-motor actuation unit with a planetary differential and holding brakes. *Mechatronics* 49: 134 – 148.
- Verstraten T, Furnémont R, Mathijssen G, Vanderborght B and Lefeber D (2016) Energy consumption of geared DC motors in dynamic applications: Comparing modeling approaches. *IEEE Robotics and Automation Letters* 1(1): 524–530. DOI:10.1109/LRA.2016.2517820.
- Verstraten T, Geeroms J, Mathijssen G, Convens B, Vanderborght B and Lefeber D (2017) Optimizing the power and energy consumption of powered prosthetic ankles with series and parallel elasticity. *Mechanism and Machine Theory* 116: 419 – 432. DOI:<https://doi.org/10.1016/j.mechmachtheory.2017.06.004>.
- Verstraten T, Mathijssen G, Furnémont R, Vanderborght B and Lefeber D (2015) Modeling and design of geared DC motors for energy efficiency: Comparison between theory and experiments. *Mechatronics* 30: 198 – 213. DOI:<http://dx.doi.org/10.1016/j.mechatronics.2015.07.004>.
- Wensing PM, Wang A, Seok S, Otten D, Lang J and Kim S (2017) Proprioceptive actuator design in the MIT Cheetah: Impact mitigation and high-bandwidth physical interaction for dynamic legged robots. *IEEE Transactions on Robotics* 33(3): 509–522. DOI:10.1109/TRO.2016.2640183.
- Wolf S and Hirzinger G (2008) A new variable stiffness design: Matching requirements of the next robot generation. In: *2008 IEEE International Conference on Robotics and Automation*. pp. 1741–1746. DOI:10.1109/ROBOT.2008.4543452.